

Extreme ultraviolet emission and confinement of tin plasmas in the presence of a magnetic field

Amitava Roy,^{1,2,a)} Syed Murtaza Hassan,¹ Sivanandan S. Harilal,¹ Akira Endo,² Tomas Mocek,² and Ahmed Hassanein¹

¹*School of Nuclear Engineering and Center for Materials Under Extreme Environment (CMUXE), Purdue University, West Lafayette, Indiana 47907, USA*

²*HiLASE Project, Department of Diode-pumped Lasers, Institute of Physics of the ASCR, Na Slovance 2, 18221 Prague, Czech Republic*

(Received 3 April 2014; accepted 12 May 2014; published online 28 May 2014)

We investigated the role of a guiding magnetic field on extreme ultraviolet (EUV) and ion emission from a laser produced Sn plasma for various laser pulse duration and intensity. For producing plasmas, planar slabs of pure Sn were irradiated with 1064 nm, Nd:YAG laser pulses with varying pulse duration (5–15 ns) and intensity. A magnetic trap was fabricated with the use of two neodymium permanent magnets which provided a magnetic field strength ~ 0.5 T along the plume expansion direction. Our results indicate that the EUV conversion efficiency do not depend significantly on applied axial magnetic field. Faraday Cup ion analysis of Sn plasma show that the ion flux reduces by a factor of ~ 5 with the application of an axial magnetic field. It was found that the plasma plume expand in the lateral direction with peak velocity measured to be ~ 1.2 cm/ μ s and reduced to ~ 0.75 cm/ μ s with the application of an axial magnetic field. The plume expansion features recorded using fast photography in the presence and absence of 0.5 T axial magnetic field are simulated using particle-in-cell code. Our simulation results qualitatively predict the plasma behavior. © 2014 AIP Publishing LLC. [<http://dx.doi.org/10.1063/1.4879825>]

I. INTRODUCTION

Extreme-ultraviolet lithography (EUVL) using photons at 13.5 nm is a major candidate for next generation lithography.¹ EUV radiation from a laser produced tin plasma has been studied extensively in recent years for its potential application as a light source for semiconductor lithography.^{2–9} A high-brightness and debris free source emitting at 13.5 nm radiation with 2% full bandwidth (in-band) is necessary for this purpose. The selection of EUV source at 13.5 nm is due to the availability of Si-Mo multilayer (ML) mirrors which reflect $\sim 70\%$ of radiation at normal incidence with a bandwidth of 2% centered at 13.5 nm. Hot tin plasmas produced by intense laser pulses heated to ~ 30 eV emit efficient EUV radiation in the in-band region.¹⁰ The power requirement for EUV lithography sources is ~ 250 W with a brightness ≥ 100 W/(mm²sr).¹¹ The essential requirements of a laser produced plasma (LPP) EUV source are a high conversion efficiency (CE; conversion from laser energy to 13.5 nm with 2% bandwidth) with minimum debris generation.

Apart from CE, the cleanliness of the EUV LPP sources is extremely important for their use in semiconductor lithography.¹² It is well known that the EUV LPP source emits debris in the form of energetic ions, atoms, and molten droplets.^{13,14} The ablated Sn vapor and debris will be deposited on various components, including the surface of the ML mirror, which causes degradation in mirror reflectivity. Several schemes proposed for mitigating the ion and atom debris, however, none of them can completely mitigate the additional damage from neutrally charged debris.^{12,13}

Ionized and neutral particle flux causes the sputtering and implantation of the debris species into the ML mirror coating, lowering its reflectivity.¹⁵ Several mitigation schemes have been proposed to improve the lifetime of the ML mirror, for example, using magnetic fields,¹⁶ a gas curtain,¹⁷ low energy prepulses,¹⁸ and mass-limited targets.^{19,20}

By applying a static magnetic field of 1 T a fivefold reduction in Sn debris deposited on Mo/Si multilayer mirror from a Sn planar target has been demonstrated.¹⁶ The debris reduction is attributed to the decrease of more than three orders in the number of ions that reach the sample mirror due to their interaction with the applied magnetic field that guides the ions away from the mirror. The remaining deposition is due to neutral Sn atoms that do not interact with the applied magnetic field.¹⁶

The effectiveness of the magnetic field ion mitigation was evaluated by measuring the erosion rate with a quartz crystal microbalance.²¹ A significant decrease of the Faraday cup (FC) signal was monitored by applying a magnetic field of 0.6 T. Target size dependence on magnetic field effectiveness was observed, measured erosion rate was reduced to less than 10% by applying 0.6 T magnetic field in the case of 10- μ m Xe jet and 300-mJ Nd:YAG laser irradiation.²¹ It was shown that with Nd:YAG laser and Sn rod target the fast ion signal decreased to $< 0.1\%$ with 1 T magnetic flux density.²² Experiments with Nd:YAG laser irradiation on Tin target showed that the kinetic energies of the plume species were considerably reduced even at short distances with a modest perpendicular magnetic field of 0.64 T.²³

Confinement and dynamics of laser-produced plasma expanding across a transverse magnetic field has been studied by many authors,^{24–29} however, there are a very few

^{a)}Electronic addresses: roy@fzu.cz and aroy@barc.gov.in

reports available for dynamics of plasma expanding along the direction of the magnetic field. An aluminum plasma created by $1.06\text{ }\mu\text{m}$, 8 ns Nd:YAG pulses was allowed to expand across a 0.64 T magnetic field.²⁴ Changes in plume structure and dynamics, enhanced emission and ionization, and velocity enhancement were observed in the presence of the magnetic field. Fast imaging studies showed that the plume is not fully stopped and diffuses across the field.²⁴ Dimonte and Wiley²⁹ investigated the magnetic profile and plasma structure during plasma expansion in a magnetic field and found that the diamagnetic cavity and plasma radii scale with magnetic confinement radius over a wide range of ion magnetization.

Three-dimensional Particle-in-Cell (PIC) simulation study of ion debris mitigation by B-field for LPP-EUV source indicates that the fast ions can efficiently be exhausted along the magnetic field without causing crucial damage to EUV collecting mirrors with the use of a single magnetic coil.³⁰ The maximum ion energy perpendicular to the magnetic field is also reduced and the ion radial flight distance becomes less than the gyro diameter estimated from the maximum energy.

Suganuma *et al.*³¹ demonstrate the principle of Electron Cyclotron Resonance (ECR) heating of laser produced Sn plasma for drift control in B field for the cleanliness of EUV light sources. The multiple-ionized plasma ions are efficiently guided along the B field lines of the double coil magnet.

In this paper, we report the effectiveness of 0.5 T axial magnetic field on EUV emission and confinement of plasma plume from a planar Sn target. Experiments are conducted for three different laser pulse widths and the laser energy has been varied from 30 mJ to 200 mJ at a laser focal spot size of $80\text{ }\mu\text{m}$. We analyzed the EUV spectral emission features, CE, ion flux and plume images with respect to laser intensity and pulse width in the presence and absence of an axial magnetic field. A particle-in cell model has been developed to represent the plasma behavior.

II. EXPERIMENTAL SETUP

A schematic of the experimental set up is shown in Fig. 1. Experiments were carried out using a Q-switched Nd:YAG laser emitting at $1.064\text{ }\mu\text{m}$ in wavelength. Pulse duration was changed from 5 to 15 ns (FWHM) by introducing a delay in the Q-switch with respect to flash lamp trigger. The laser beam energy was attenuated using a combination of a half-wave plate (WP) and a polarizing cube. Planar slab of pure Sn was mounted to a servomotor controlled XYZ translation stage inside a stainless steel high-vacuum chamber. The chamber is evacuated using a turbomolecular pump to a pressure lower than 10^{-5} Torr. A 40 mm plano-convex focusing lens was mounted on a micrometer actuator controlled x-translation stage that allowed tunability of the laser spot size. Laser focal spot diameter employed in the experiment was $80\text{ }\mu\text{m}$. The target was translated between shots to refresh the target surface, and to mitigate the effects of target cratering. The beam energy was monitored using an energy meter.

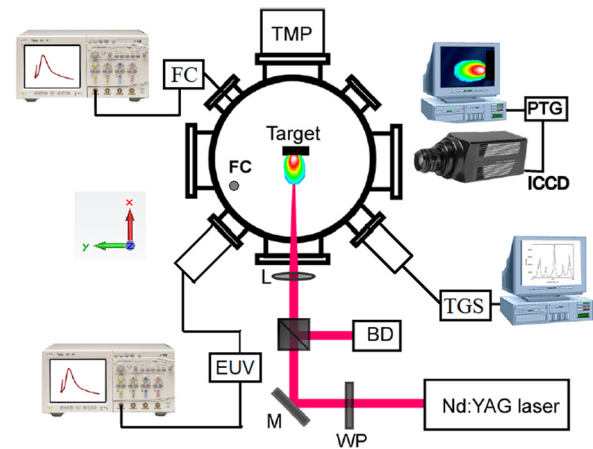


FIG. 1. Schematic of the experimental setup is given. Optical components include a polarizing cube (C), a half-WP, lens (L), mirror (M), and beam dumps (BD). Diagnostic components include a FC; and TGS, ICCD camera and EUV power tool. The magnetic field is applied along the plume expansion direction (z-direction).

The CE of the incident laser pulse energy to 13.5 nm radiation was measured using a EUV power tool which consists of two Zr filters and a Mo/Si ML mirror to reflect the incoming EUV in-band radiation into an absolutely calibrated photodiode. The photodiode signal is then displayed and recorded on a 1 GHz oscilloscope. The planar target geometry emits EUV radiation through a solid angle of 2π steradians. The emission spectrum of Sn plasma was recorded using a transmission grating spectrometer (TGS). The TGS utilizes a silicon nitride diffraction grating with 10 000 lines/mm resolution. The spectra were then recorded with EUV sensitive charge coupled device (CCD) camera (Princeton Instruments PIXIS) in a time-integrated manner. The TGS and energy monitors were located 90° with respect to target normal and the laser angle of incidence (AOI) is 66° . Experimental schematic shows the top view therefore the AOI is not clear in the Fig. 1.

The fluence and kinetic energy (KE) of the plasma ions were measured using a Faraday cup (FC, Kimball Physics Inc. model no. FC-71 A) mounted inside the vacuum chamber at a distance 15 cm from the target point, at 66° angle from the target normal. The FC has an entrance aperture of 3 mm in diameter and 2.54 mm^2 plate size. The ion current was measured by acquiring the voltage signal across a load resistor by 1 GHz digital phosphor oscilloscope (Agilent D8104).

A magnetic field setup was employed for performing EUV generation and plume confinement studies. Two neodymium magnets ($5\text{ cm} \times 2.5\text{ cm} \times 1.5\text{ cm}$) with a maximum field of 1.3 T were used for making the magnetic field setup. The separation between the magnets was kept at 2.3 cm. The target is placed at a distance of 0.47 cm from the pole edge in the Z direction such that the magnetic field at the target is $\sim 0.5\text{ T}$. The magnetic field distribution in the plasma plume expansion area is given in Fig. 2.

The plume imaging was accomplished using an intensified charged coupled device (ICCD, PI MAX) placed orthogonal to the plasma expansion direction. A Nikon objective lens was used to image the plume region onto the camera to

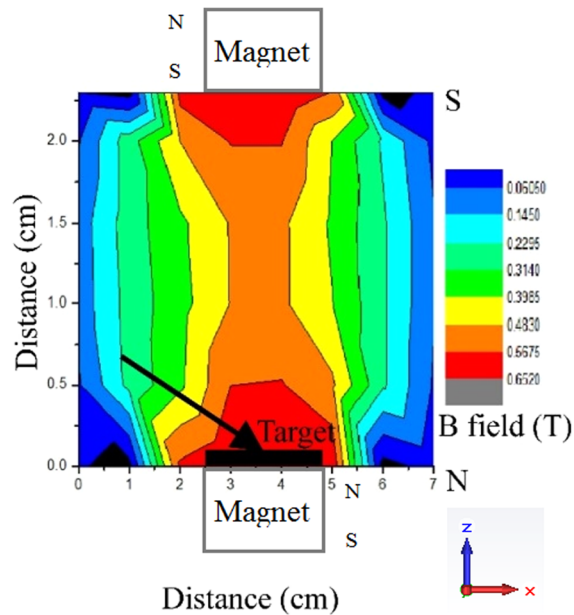


FIG. 2. The magnetic field distribution between the two magnets at the plasma plume expansion area separated by 2.3 cm measured using a Gauss meter. The arrow represents the laser direction. The laser angle of incidence was 66° and the plume expanded normal to the target surface (z-axis).

form a two-dimensional image of the plume intensity. The visible radiation from the plasma was recorded integrally in the wavelength range 350–900 nm. A programmable timing generator was used to control the delay time between the laser pulse and the imaging system with overall temporal resolution of 1 ns.

III. RESULTS AND DISCUSSION

A. EUV emission

We evaluated the unresolved transition array (UTA) and CE of in-band radiation from laser produced Sn plasma at various pulse durations and laser intensities with and without the magnetic field. The dependence of in-band CE for three different laser pulse widths (5 ns, 10 ns, and 15 ns) are studied for various laser intensities and the results are given in Fig. 3(a). We monitored the EUV emission at 90° with respect to the target normal. The self-absorption properties of the plasma changes with plasma temperature and density and hence more re-absorption can be expected at the wings because of the presence of colder plasma. The maximum CE is measured for 5 ns pulse width. Previous studies showed that the EUV radiation from laser-produced plasma from a solid target has a strong angular dependence.³² The measured CE ($\sim 1.2\%$) is found to be significantly lower compared to the CE measurements performed at 45° to the target normal ($\sim 2\%$).³³ This could be due to changes in plasma opacity with angle of observation.⁹ It should be noted that we are estimating CE by integrating over 2π sr by assuming the EUV radiation is isotropic. However, Morris *et al.*³² reported that the in-band emission intensity was relatively constant up to an angle of 60° from the target normal, beyond which it dropped steeply.

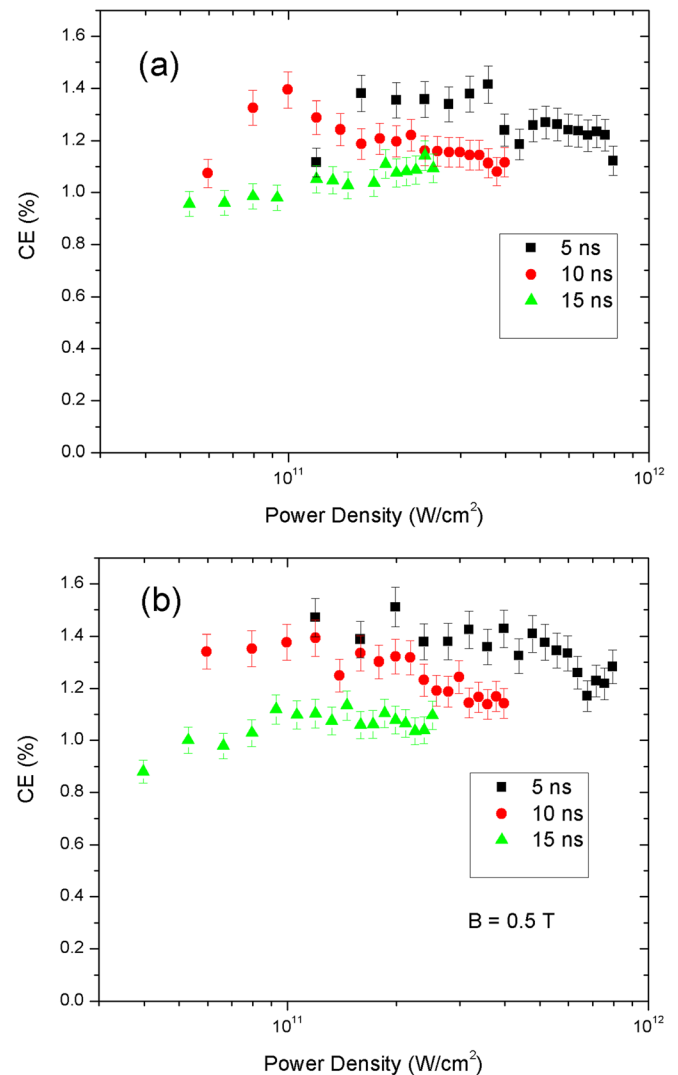


FIG. 3. The dependence of CE on laser intensity for various laser pulse width recorded at 90° with respect to target normal (a) without magnetic field (b) with 0.5 T axial magnetic field. For the CE measurement, the power tool was positioned at 90° with respect to target normal and integrated over 2π assuming EUV emission is isotropic.

Fig. 3(b) displays the result of the same experiment repeated in the presence of an axial magnetic field. One can see that there is no significant difference in the measured CE with and without magnetic field for various laser pulse widths and intensities. Therefore, an axial magnetic field with respect to the direction of plasma plume expansion does not have any significant effect on CE from planar Sn target. It is well known that the EUV emission predominantly emits only during the laser pulse interaction with Sn target. The plasma pressure during that time is significantly higher compared to any pressure exerted by the B field. Therefore, one can expect that a magnetic field may not have any significant effect on CE.

EUV spectra for three different laser pulse widths were recorded in the presence and absence of 0.5 T magnetic field at 80 mJ laser energy, and are given in Fig. 4. The spectral intensities for all the pulse widths are identical with and without magnetic field. Previous reports showed a dip in the center of the UTA (13.5 nm) and attributed to re-absorption of 13.5 nm light by the surrounding plasma.³⁴ However, such

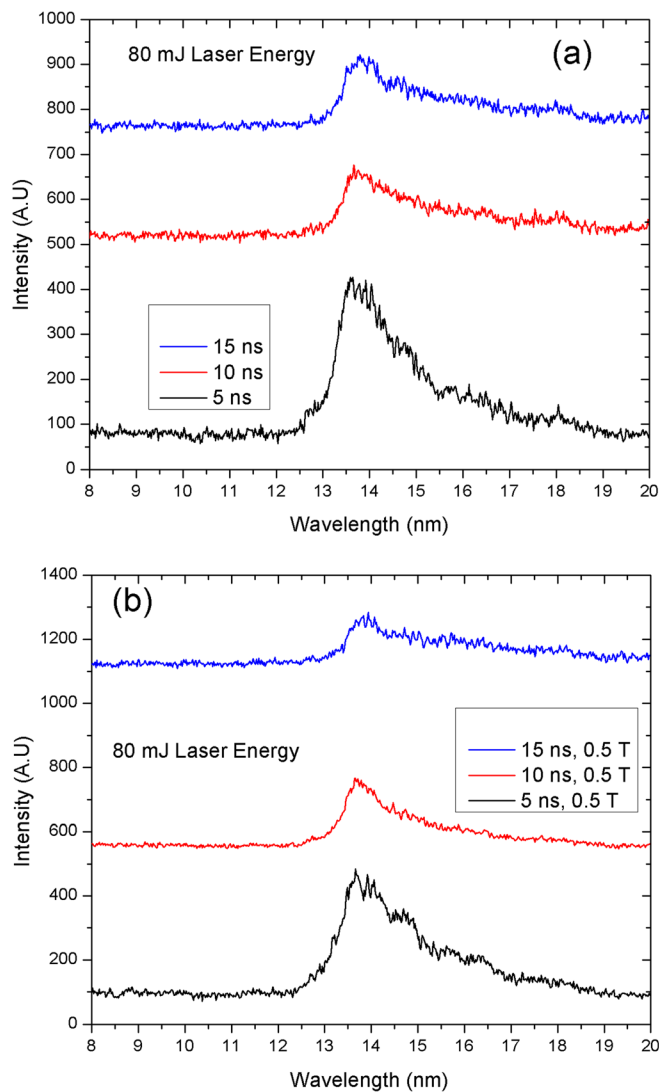


FIG. 4. EUV spectra (single-shot) for three different laser pulse width recorded with laser pulses of 80 mJ energy (a) without magnetic field (b) with 0.5 T magnetic field. For UTA recording, the TGS was positioned at 90° with respect to target normal. There is no significant difference in the EUV spectra with and without a guiding magnetic field for various laser pulse width and intensity.

a dip structure around 13.5 nm is not very prominent for any of the recorded spectra, i.e., the re-absorption of the plasma is in our case high.

B. FC ion analysis

We used a FC for evaluating the role of magnetic field on the ion emission from LPP. FCs are one of the simplest methods for analyzing ions from LPPs. However, they provide an integrated ion signal containing all charge states, and also space charge effects could distort the FC signal.³⁵ Nevertheless, it is a very useful tool for obtaining the integrated ion flux, the velocity of the ions, and hence, the KE distribution.

Previous studies¹⁶ using a CO₂ laser on FC analysis on LPP show fast Sn ions having most probable energy of 0.9 keV with a maximum energy of around 4 keV. These ions consist of low charge states due to recombination. Fast

ions are produced as a result of the acceleration caused by charge separation during their expansion into vacuum.^{12,36} The Sn deposition rate on the Mo/Si multilayer mirror depends, on the fast ion energy distribution, which is attributed to the plasma parameters originating from the laser and target parameters.¹⁶ The fast ion number versus the magnetic field strength was evaluated from the Faraday cup signal. In the case of an applied axial magnetic field of 1 T, the Sn ion flux decreased by more than three orders of magnitude.¹⁶

Experiments were conducted with Nd:YAG laser generated Sn plate target plasma in the presence and absence of 1 T magnetic field and results showed that the FC signal decreased below the detection limit (about 3 orders) in the presence of magnetic field.³⁷ It was reported that for Nd:YAG LPP, the ions only weakly influence the deposition.³⁷ From the experimental results, it is estimated that the ion effect on deposition is below 1%. In case of a Nd:YAG drive laser and a Sn target, debris mitigation is therefore much more important than ion mitigation.³⁷

The ion time-of-flight (TOF) profiles are represented by a sharp prompt peak, followed by a broad slower peak.¹² The fast prompt peak in the ion signal is caused by the photoelectric effect and can be used as a time marker.¹² Figure 5 shows the TOF signals obtained at fixed laser intensity for two different laser pulse widths with and without magnetic field. For this measurement, the FC was positioned at 15 cm from the plasma at an angle of 66° with respect to target normal. The

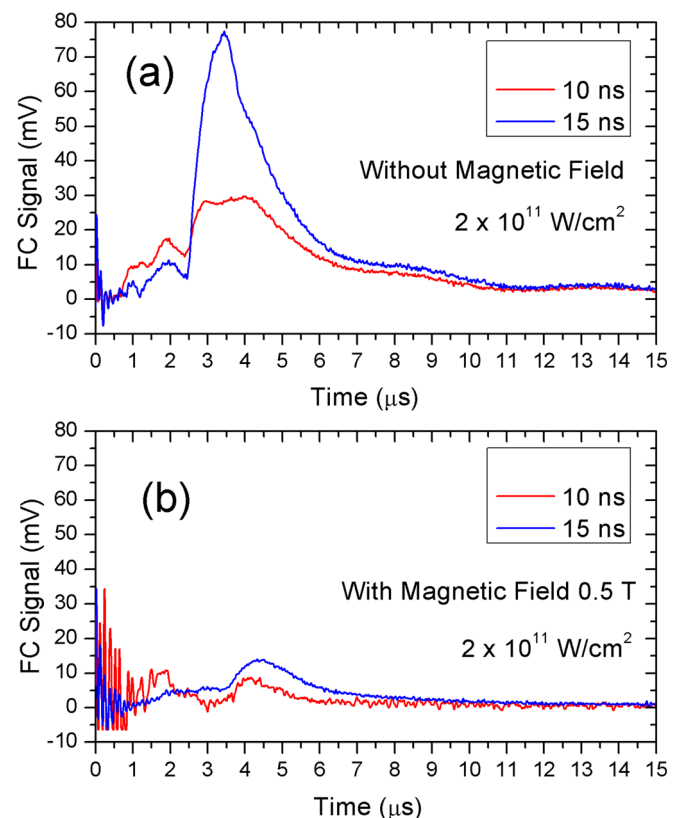


FIG. 5. The TOF ion signal (single-shot) for two different laser pulse width. (a) Without magnetic field, (b) with a magnetic field. For these measurements the FC is positioned at 15 cm from the target at an angle 66° from the target normal. The laser intensity used in this measurement was $2.0 \times 10^{11} \text{ W/cm}^2$.

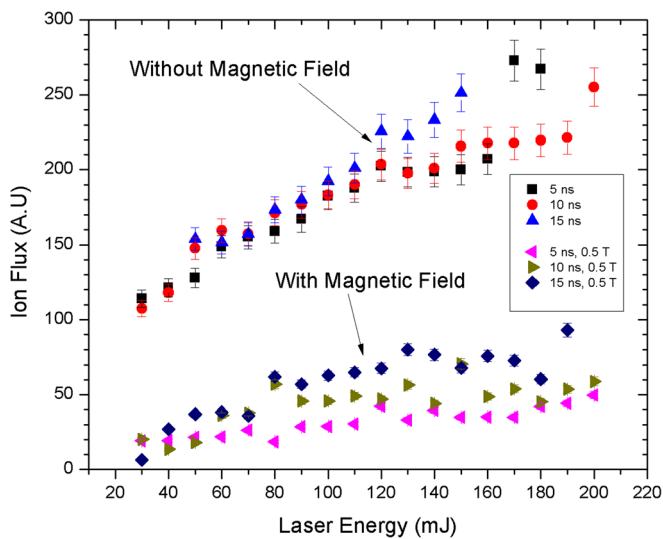


FIG. 6. The estimated ion flux as a function of laser energy for three different laser pulse width with and without an axial magnetic field. For these measurements the FC is positioned at 15 cm from the target at an angle 66° from the target normal.

estimated most probable ion KE from TOF signal for 80 mJ, 5 ns laser pulse without magnetic field is 1.2 keV. It can be seen from Fig. 5 that the FC signal is reduced by ~ 5 times with the application of the magnetic field.

Figure 6 displays the measured ion flux for three different laser pulse widths for various laser energies with and without a magnetic field. To obtain the ion flux (number) from the FC signal the average charge state is needed but not for a relative analysis as presented in Fig. 6. However, the same average charge state is assumed for the result displayed in Fig. 6. One can see from the Fig. 6 that ion flux increases with laser energy. The ion flux remains more or less constant regardless of laser pulse width. Ion flux reduced by ~ 5 times with the application of 0.5 T magnetic field. It is interesting to note that the ion flux keep on increasing with the laser energy without the magnetic field. However, the rate of increase of ion flux with laser energy reduces significantly with the application of the magnetic field. The difference in the ion flux for various laser pulse width becomes prominent with the magnetic field and steadily increase with the laser pulse duration.

C. Plasma plume dynamics

Fast photography using an ICCD provides two-dimensional snapshots of the three-dimensional plume

propagation. These images provide valuable insight into the hydrodynamic expansion of plasma plumes, as well as radiation emission. The colors in the ICCD camera images indicate different radiation intensity values. Higher counts observed in the images correspond to areas of high temperature and particle density in the plasma plume. Therefore, this technique provides details of the expansion dynamics of the plasma.³⁸

Recorded plasma images at various times of its evolution in the presence and absence of magnetic field are given in Fig. 7. The duration of the intensification (exposure time) is 10 ns and each image is obtained from a single laser pulse of 130 mJ and 5 ns duration. Timing jitter is less than 1 ns. All of the images given in the figures are normalized to the maximum intensity in that image. It should be remembered that each image represents the spectrally integrated plume in the region at 350–900 nm that is due to emission from the excited states of various species (i.e., charge and excitation states) and are normalized to maximum intensity of each image for a clear view. They are not necessarily representative of the total flux because a part of the plume is nonluminous.

The application of laser beam on Sn target in vacuum creates an intensely luminous plume that expands normal to the target surface. Initially hemispherical plasma was formed with respect to the target surface. The plume expands freely in vacuum environment and is simply adiabatic and can be fully predicted by theoretical models.^{36,39} With the presence of axial magnetic field, guiding of the plasma along the field lines are observed. The images also show a collimating effect on the expanding plasma. The estimated maximum expansion velocity of the magnetically confined plasma from the images is ~ 4.0 cm/ μ s. A secondary plasma formed on the opposing magnet also visible in the images. This may be caused by fast moving ions. The plume lifetime is found to increase in the presence of the magnetic field. When the plasma thermal pressure $P_t = n_0 k T_e$ exceeds the magnetic pressure $P_B = B_0^2 / 2\mu_0$ the plasma plume start diffuse in to the magnetic field in the lateral direction and expands until the plasma and magnetic pressures equalize.

One can see from the Fig. 7 that the shape of the plume changes significantly in the presence of the magnetic field. The plasma expands freely in the direction of the magnetic field lines, however, a sharp boundary forms between the plasma and the magnetic field in the lateral direction. Figure 8 displays the position-time ($R(z) - t$) plot obtained from the imaging data with and without a magnetic field.

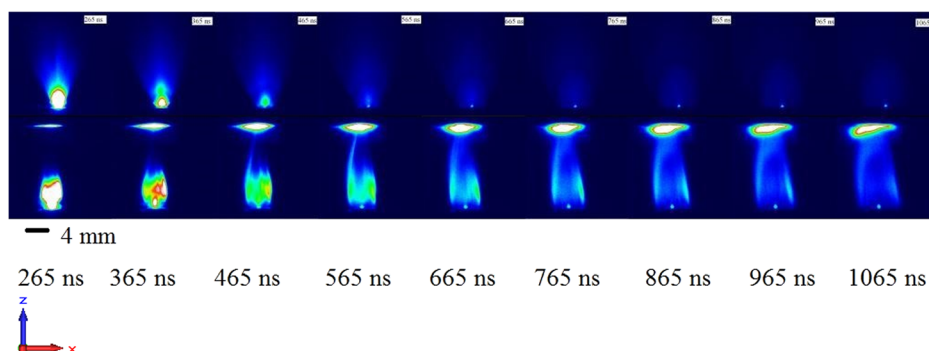


FIG. 7. Plume images recorded using 10 ns gated ICCD camera in the presence (bottom) and absence (top) of the axial magnetic field. The times in the figure represent the time after the evolution of the plasma. For better clarity, each image is normalized to its maximum intensity. A secondary plasma formed on the opposing magnet also visible in the images. This may be caused by fast moving ions.

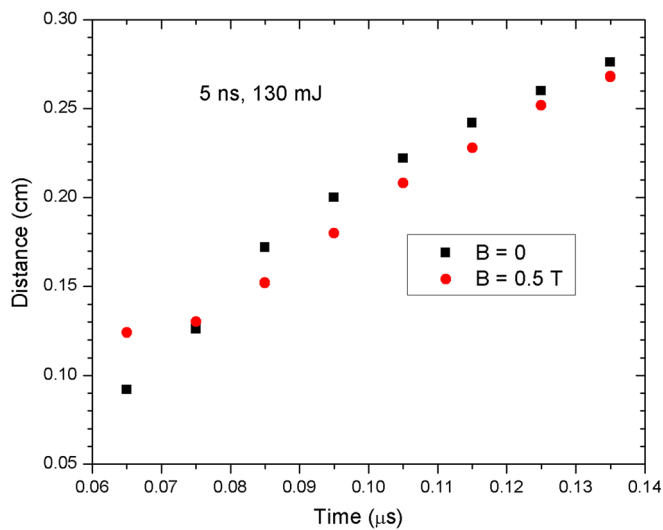


FIG. 8. $R(z)$ - t plots obtained from plume images. Plume expansion in the axial direction remains identical with a magnetic field. The laser parameter used in this experiment was 5 ns, 130 mJ with 80- μ m spot size.

The axial expansion velocities of the plasmas can be measured from the slopes of the displacement-time graph. The expansion velocity of the plume remains almost same when an axial magnetic field is applied. The estimated expansion velocity was 4 cm/ μ s. In vacuum, the plume boundary is not so sharp and therefore one can expect 15%–20% error in plasma velocity estimation. The ICCD images showed lateral confinement and the B lines are guiding the plasma. When the pressure of the plasma is greater than the magnetic pressure, the plasma is expected to penetrate through the region occupied by the magnetic field. Plasma confinement and stagnation take place when the magnetic and plasma pressures balance. Figure 9 displays the estimated plume diameter (widest cross section of the plasma plume) at three different axial distances from the Sn target with and without a magnetic field for the same laser parameters as in the Figs. 7 and 8.

One can see from the Fig. 9 that at 1 mm distance, the plume width is lower without a magnetic field and increases slowly with time. The peak expansion velocity of the plasma plume in the lateral direction at a distance 1 mm from the target is ~ 1 cm/ μ s. With the application of the magnetic field the peak expansion velocity reduces to ~ 0.9 cm/ μ s. One can see from the Fig. 9(b) that the plume width reduces significantly with the application of a magnetic field especially at farther distances from the target. The peak plume expansion velocities ~ 1.2 cm/ μ s without the magnetic field, however, reduced to ~ 0.65 cm/ μ s with the magnetic field. At 6 mm from the target surface the plume diameter reduces by a factor of 1.75 with the magnetic field. The plume becomes polarized due to the Lorentz force which in turn creates an electric field that causes the entire plasma to $\mathbf{E} \times \mathbf{B}$ drift across the background magnetic field as described by Borovsky.⁴⁰ In previous studies the plasma plume is observed to narrow or “focus” in the plane perpendicular to the field, while in the plane of the field the plasma expands along the field lines and displays flutelike striations.²⁶ The narrowing of the plasma plume is explained in terms of the configuration of the plasma polarization fields,

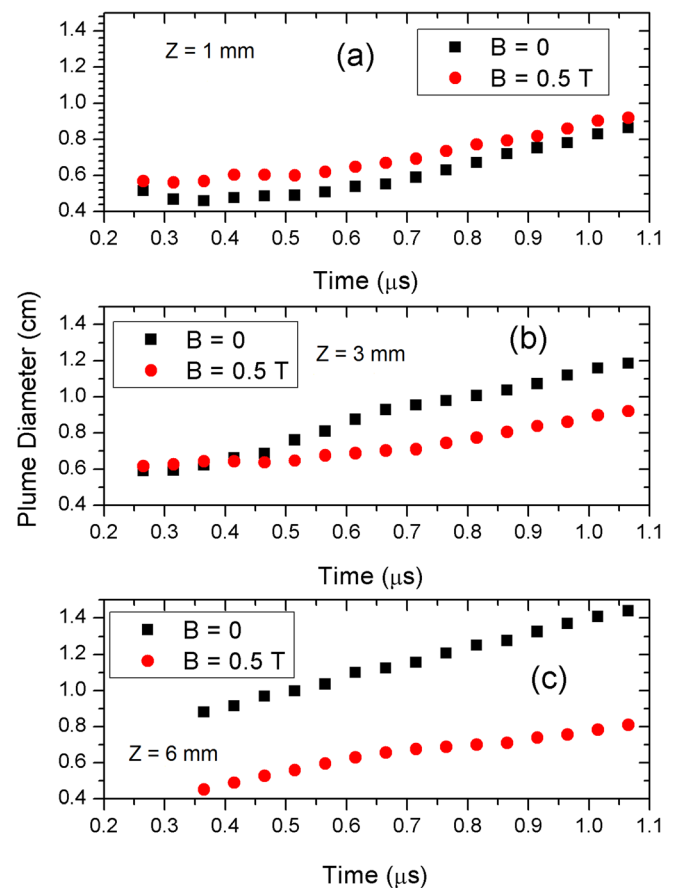


FIG. 9. Plume diameter obtained from images with and without a magnetic field for the distances from the target (a) 1 mm, (b) 3 mm, and (c) 6 mm.

while the flute structure is identified as an electron-ion hybrid velocity-shear instability.²⁶ However, compared to the present experiment, the magnetic pressure in Ref. 26 is much larger than the thermal and ram pressures and hence diamagnetic currents are weak. Recent experiments by Plechaty *et al.*²⁷ showed that a plasma plume preferentially expanding along the target normal in the absence of a magnetic field is confined laterally and turns into a directed plasma flow when a field is applied. The lateral confinement leads to a redirection of the interior plasma originating from the target region heated by the ablation laser. The magnetic pressure redirects the flow toward the axis, and this convergence generates a directed flow. However, the laser energy and external magnetic field in Ref. 27 was extremely high ~ 8 J and 7 T near the target surface, respectively.

At 6 mm from the target surface the lateral peak plume expansion velocity measured to be ~ 1.2 cm/ μ s and ~ 0.75 cm/ μ s without and with an axial magnetic field, respectively. Therefore, with the application of a 0.5 T magnetic field the plasma plume expansion velocity reduces by a factor of 1.6 in the lateral direction.

The maximum velocity of ions measured from FC was 4.4 cm/ μ s, which was marginally higher than the velocity 4.0 cm/ μ s of plume in axial direction estimated by the ICCD images. It implies that the fast moving ions in the plasma plume are not emitting in the visible region of the electromagnetic spectrum.

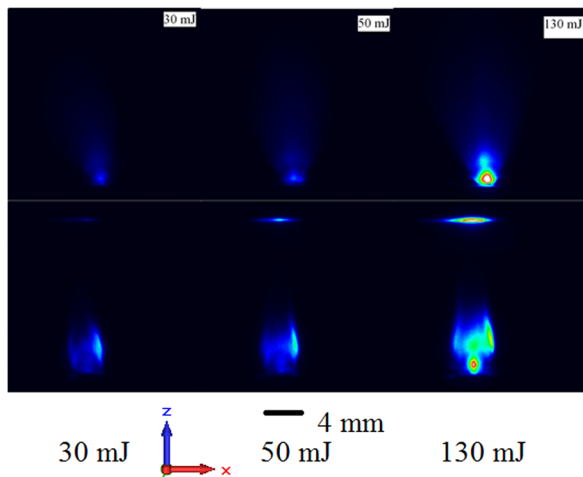


FIG. 10. Plume images recorded at 315 ns time delay for 5 ns laser pulse width but different laser energies in the presence (bottom) and absence (top) of the axial magnetic field. The laser spot size was $80\ \mu\text{m}$ in diameter. For better clarity, each image is normalized to its maximum intensity. The laser intensities are 1.19×10^{11} , 2.0×10^{11} , and $5.17 \times 10^{11}\ \text{W/cm}^2$, respectively.

We have also studied the Sn plume images for various laser energies and pulse widths in the presence of a magnetic field. Figure 10 displays the plume images recorded at a time delay of 315 ns for 5 ns pulse width for various laser energies.

One can see from the Fig. 10 that as the laser energy increases the plume becomes brighter. The plasma plume is getting brighter with increasing laser energy suggests higher temperature which leads to enhanced collision with the charged species. Figure 11 displays the effect of laser pulse width on plume images for a fixed laser energy 30 mJ with and without a magnetic field. One can see from the Fig. 10 that plasma plume is getting brighter as the laser pulse duration increases.

Figure 12 shows the plasma plume recorded at a fixed laser intensity $2 \times 10^{11}\ \text{W/cm}^2$ for 5 ns, 10 ns, and 15 ns pulse

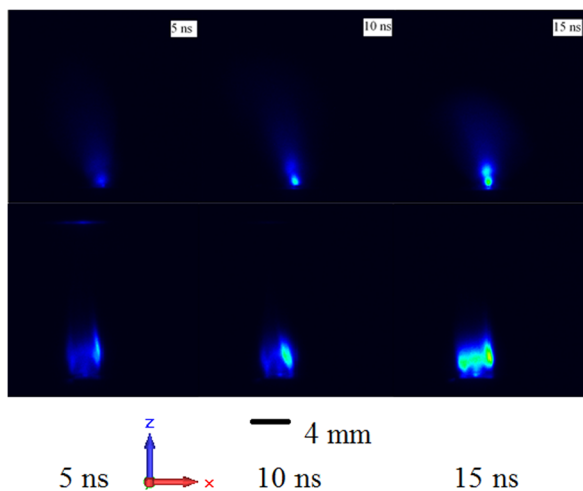


FIG. 11. Plume images recorded at 315 ns time delay for various laser pulse width at a fixed laser energy 30 mJ in the presence (bottom) and absence (top) of the axial magnetic field at $80\ \mu\text{m}$ spot diameter. For better clarity, each image is normalized to its maximum intensity. The laser intensities are 1.19×10^{11} , 5.97×10^{10} , and $3.98 \times 10^{10}\ \text{W/cm}^2$, respectively.

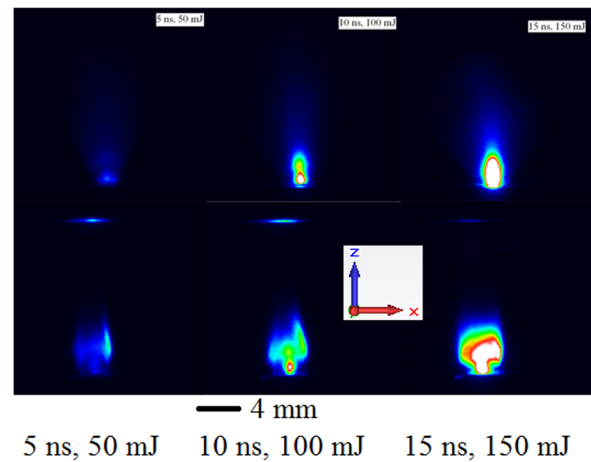


FIG. 12. Plume images recorded at 315 ns time delay for various laser pulse width at fixed laser intensity $2 \times 10^{11}\ \text{W/cm}^2$ in the presence (bottom) and absence (top) of the axial magnetic field at $80\ \mu\text{m}$ spot diameter. For better clarity, each image is normalized to its maximum intensity.

durations with and without the magnetic field. It can be seen that the plasma plume is getting bigger and brighter with the increase in laser pulse duration at a fixed intensity.

D. Particle in cell simulation

PIC⁴¹ simulation is a powerful tool for predicting plasma behaviors produced by lasers. The PIC algorithm simulates the motion of each sample plasma particle calculating at each time step the macro quantities with it associated: current density, pressure, velocity of the particles. Modern codes can simulate up to 10^{10} particles and follow the motion of plasma in a complicated system.

Expansion dynamics of laser produced spherical plasma has been studied by using 3D PIC method.³⁰ The maximum ion energy in free expansion of the plasma and its dependence on plasma parameters has been studied and the validity of B-field shield concept in LPP-EUV source has been established. The maximum ion energy is shown to be determined from the plasma size parameter. It was shown that the ion radial flight distance is reduced less than the maximum gyro diameter by applying an external magnetic field. The fast ions can be guided along the magnetic field lines efficiently with the use of a single magnetic coil.³⁰

We have used the CST Particle Studio (PS)⁴⁴ PIC code to simulate the plasma expansion in vacuum with and without a magnetic field. The PIC solver, which works in the time domain, can perform a fully consistent simulation of particles and electromagnetic fields. The mutual coupling between particles and electromagnetic fields is taken into account in this self-consistent relativistic PIC code. With several emission models such as Direct Current (DC), series of Gaussian bunches, field emission and user defined emissions, and virtually any particle source can be modeled. The particles can interact with a combination of electrostatic, magnetostatic, eigenmode, transient electromagnetic, and user-defined fields.

In an optimized Nd:YAG LPP EUV source, the electrons are heated to 30 eV and expand into vacuum. Ions are then accelerated due to the electric field generated by

TABLE I. A comparison between the plasma PIC simulation parameters and experimental parameters from reported literature.^{42,43}

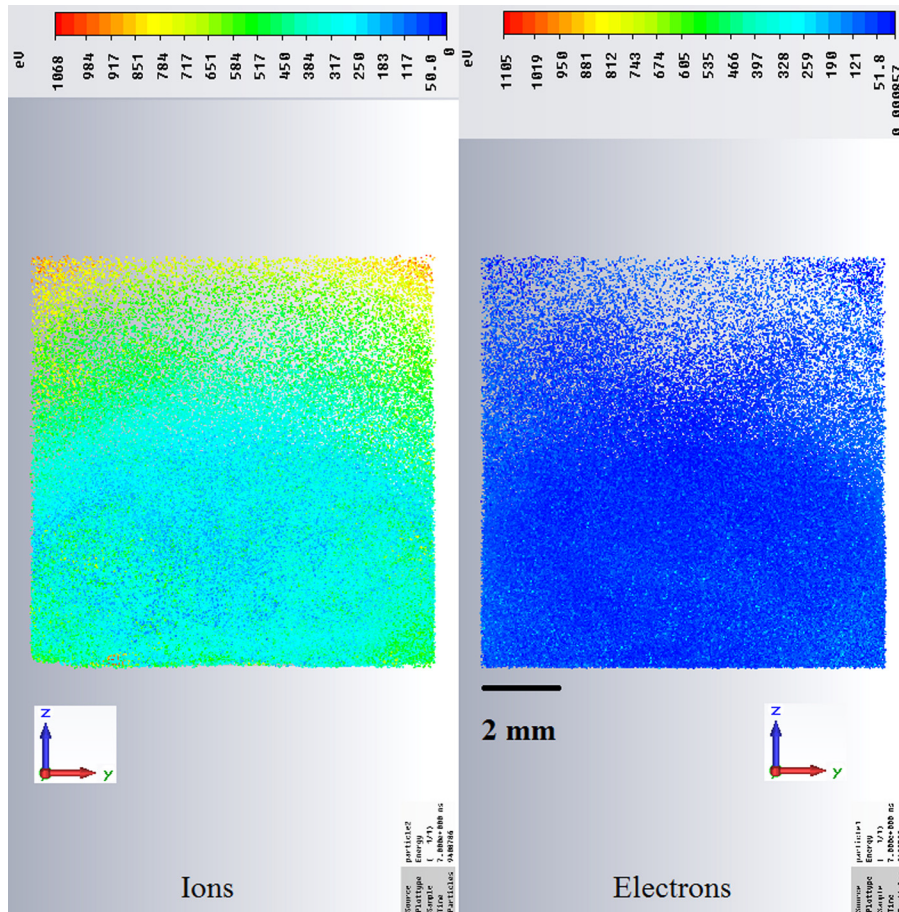
| Parameters | Experiment | CST Simulation |
|---|------------------------------------|------------------------------------|
| Initial electron temperature (T_e) | 30 eV | 30 eV |
| Initial ion temp. | 0 | 0 |
| Initial electron density (n_e) | $5 \times 10^{16} \text{ cm}^{-3}$ | $5 \times 10^{16} \text{ cm}^{-3}$ |
| Mass ratio (m_i/m_e) | 2.16×10^5 | 100 |
| Ion plasma frequency (ω_{pi}) | 2.74×10^{10} | 1.27×10^{12} |
| Debye length (λ_D) | $1.8 \times 10^{-7} \text{ m}$ | $1.8 \times 10^{-7} \text{ m}$ |
| Magnetic field | 0.5 T | 0.5 T |
| Charge state (Z) | +1 to +13 | +1 |
| Initial pressure ratio (β) | 2.46 | 2.46 |
| Initial plasma radius | 40 μm | 40 μm |
| Ion acoustic velocity (C_s) | $4.9 \times 10^3 \text{ m/s}$ | $2.3 \times 10^5 \text{ m/s}$ |
| Time scale | 47 ns | 1 ns |
| Ion Larmor radius ($E_i = 1.2 \text{ keV}$) | 10.8 cm | 0.23 cm |

expanding electrons. We evaluated the maximum ion kinetic energy for an electron ion plasma with uniform density n_0 and finite electron temperature T_e and ion temperature $T_i = 0$ with the use of 3D PIC code CST PS. A simulation volume of $10 \text{ mm} \times 10 \text{ mm} \times 10 \text{ mm}$ with total number of particles $> 2 \times 10^7$ has been used. The total numbers of meshshells used are 569 492. A static homogeneous magnetic field of $B_z = 0.5 \text{ T}$ used in the simulation. We have used the ion-electron mass ratio of $m_i/m_e = 100$ to reduce the simulation

time.^{30,45} It should be noted that even if we use a present day super computer, it is still very difficult to simulate plasma expansion using real ion-electron mass ratio.³⁰ Therefore, in the PIC simulation we use fictitious values keeping important physics to be the same. Table I displays the plasma simulation parameters^{42,43} and a comparison with the reported experimental parameters for the similar experimental conditions used in the present experiment.

Figure 13 displays the ion and electron motion and respective energies at real time $\sim 329 \text{ ns}$. One can see that the plasma particles cover almost all the simulation space and the maximum energy of the ion reaches $\sim 1 \text{ keV}$. We measured similar maximum KE of Sn ions in our previous experiments.³³ However, the energy of the electrons in the present simulation is quite low at this time and maximum energy observed $\sim 300 \text{ eV}$.

Figure 14 displays the ion and electron motion and respective energies at real time $\sim 329 \text{ ns}$ with 0.5 T axial magnetic field. One can see from Fig. 14 that the plasma particles are confined in the axial direction. Motions of the plasma particles are same as observed in the experiment (Fig. 7). In this case the ions acquire a maximum energy of $\sim 1.3 \text{ keV}$ and observed at the tail end of the particle motion. Whereas the maximum energy of the electrons is $\sim 1 \text{ keV}$, which is little higher than that without magnetic field. Therefore, with the application of an axial magnetic field both the plasma electrons and ions acquire slightly higher energies.

FIG. 13. A snap shot of ion and electron motion at $\sim 329 \text{ ns}$ in real time. The line colors in the picture represent energy of the particles.

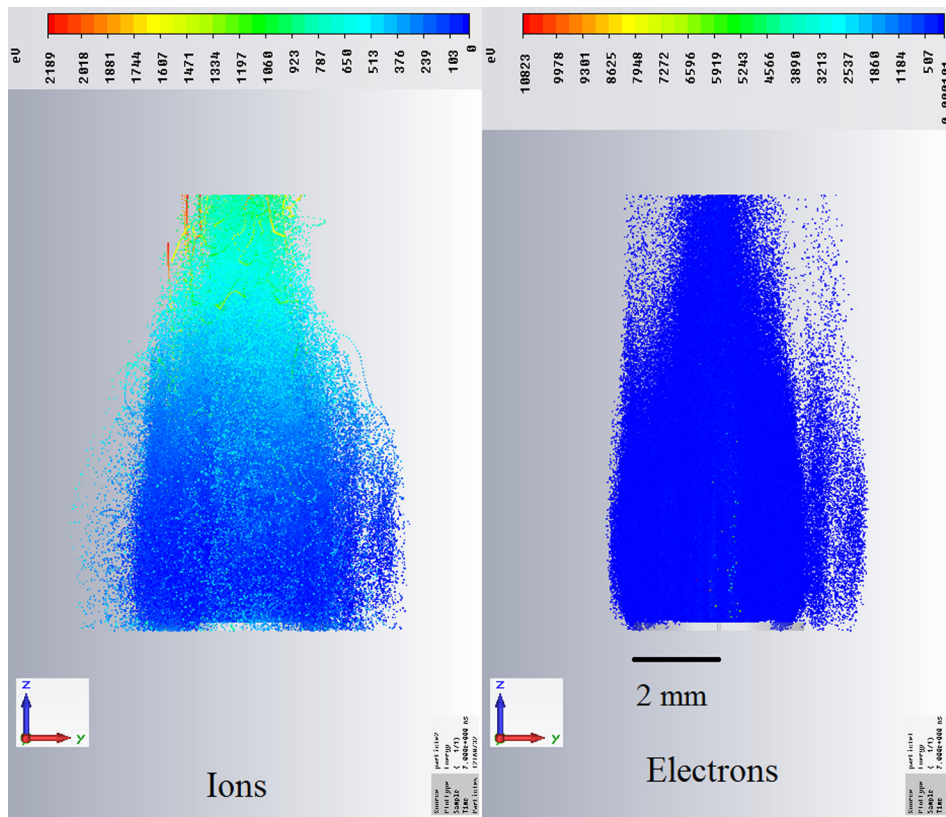


FIG. 14. A snap shot of ion and electron motion at ~ 329 ns in real time with 0.5 T axial magnetic field. The line colors in the picture represent energy of the particles.

Figure 15 shows the phase space diagram of the plasma particles in the presence and absence of axial magnetic field. In this figure particle energies are plotted with respect to Y .

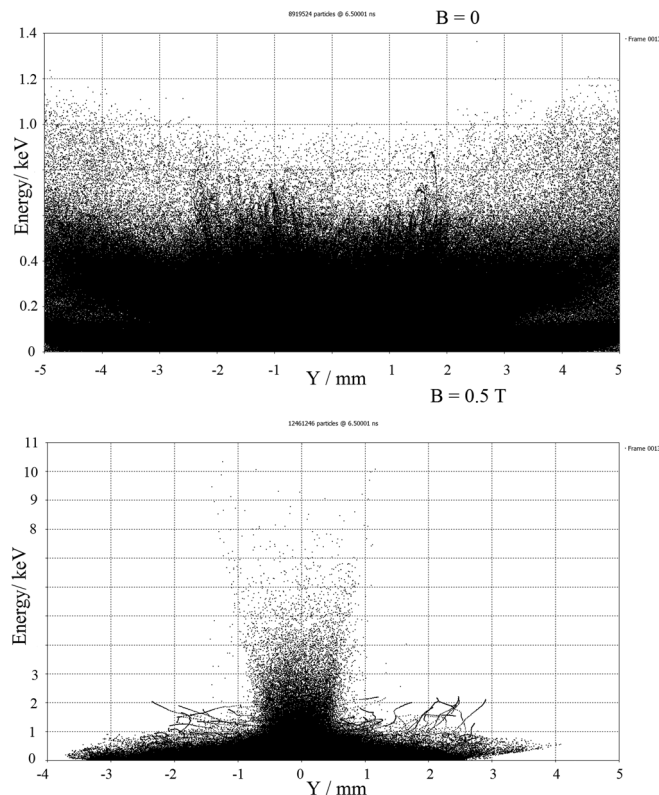


FIG. 15. The phase space diagram of the plasma particles with and without a magnetic field with respect to dimension parallel to the target plane at ~ 305 ns.

One can see that with the application of magnetic field particles acquire much higher energies near the center close to the laser spot.

Figure 16 displays the phase space diagram of the plasma particles with and without a magnetic field with Z . The energy of the particles without the magnetic field remains < 800 eV close to the target, however, increases to ~ 1.1 keV as we move away from the target. In the case of 0.5 T magnetic field the plasma particles acquire much higher energy ~ 8 keV near the target but have lower kinetic energy at larger distances from the target. At a distance of 10 mm from the target the particle energy reduced to 2 keV. As can be seen from the Fig. 14 that the result is not symmetric, probably due to some instability of the plasma. At large Z the energy of the ions are in the range of 0.8 to 2 keV. One can also see from Fig. 16 for $B = 0$ T at 10 mm from the target, three separate “energy bands” are to be seen. It is clear from the Fig. 14 that the top energy band is due to the ions as at 10 mm from the target electrons are having much lower energy than ions.

IV. SUMMARY

We investigated the role of axial magnetic field on EUV spectral emission, CE and ion emission features of laser produced Sn plasma. It was found that the present axial external magnetic field configuration of 0.5 T has no significant effect on the CE of the EUV radiation. This is expected because of the fact that the EUV emission occurs predominately during the laser pulse interaction with the Sn Target. However, during this time the plasma pressure is very high as compared to the pressure exerted by the magnetic field due to very high

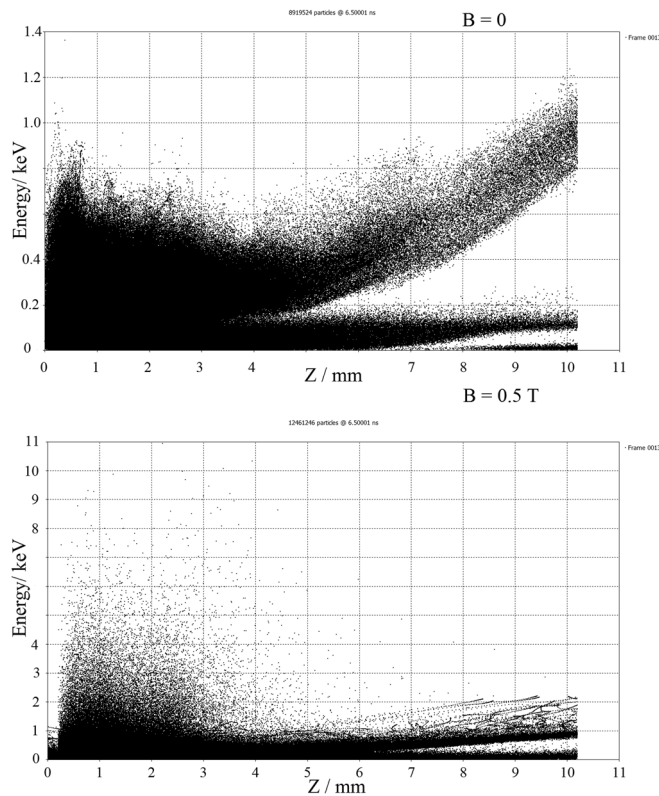


FIG. 16. The phase space diagram of the plasma particles with and without a magnetic field with respect to dimension perpendicular to the target plane at 305 ns.

temperature (~ 30 eV) produced by the laser interaction with the Sn target materials.

FC analysis of Sn plasma ion emission was used to generate ion and KE profiles. It was found that the ion flux is reduced by ~ 5 times with the application of the magnetic field. The ion flux increases with laser energy. The ion flux remains more or less constant regardless of laser pulse width.

Details of the expansion dynamics of the plasma was obtained using ICCD two-dimensional snapshots of the three-dimensional plume propagation. The expansion velocity remains the same regardless of the applied axial magnetic field. In the presence of axial magnetic field, guiding of the plasma along the field lines are observed. The plume lifetime is found to increase in the presence of the magnetic field. The lateral peak plume expansion velocity measured to be ~ 1.2 cm/ μ s and ~ 0.75 cm/ μ s without and with an axial magnetic field, respectively. Therefore, with the application of a 0.5 T magnetic field the plasma plume expansion velocity reduces by factor of 1.6 in the lateral direction of plume expansion. It was also found that plasma plume is getting bigger and brighter as the laser pulse duration increases for a fixed laser energy as well as intensity due to increase in plasma temperature.

The expansion dynamics of the laser-produced plasma has been simulated by 3D PIC code CST Particle Studio. It was found that the laser produced plasma behavior could be qualitatively predicted by the PIC method. PIC simulation reveals that the application of a magnetic field increases both the electron and ion energies close to the laser focal spot.

The guiding magnetic field can be an effective method to reduce the ion debris by guiding through the magnetic field lines to an ion dump without affecting the CE.

ACKNOWLEDGMENTS

This work was supported in part by the U.S. National Science Foundation (PIRE project) and co-financed by the European Regional Development Fund, the European Social Fund and the state budget of the Czech Republic (Project HiLASE: CZ.1.05/2.1.00/01.0027, Project DPSSLasers: CZ.1.07/2.3.00/20.0143, Project Postdok: CZ.1.07/2.3.00/30.0057).

- ¹V. Bakshi, *EUV Lithography* (SPIE and John Wiley & Sons, Inc., Bellingham, WA/Hoboken, NJ, 2009).
- ²J. White, G. O'Sullivan, S. Zakharov, P. Choi, V. Zakharov, H. Nishimura, S. Fujioka, and K. Nishihara, *Appl. Phys. Lett.* **92**, 151501 (2008).
- ³J. White, P. Dunne, P. Hayden, and G. O'Sullivan, *J. Appl. Phys.* **106**, 113303 (2009).
- ⁴S. Yuspeh, K. L. Sequoia, Y. Tao, M. S. Tillack, R. A. Burdt, and F. Najmabadi, *Appl. Phys. Lett.* **96**, 261501 (2010).
- ⁵Y. Ueno, G. Soumagne, A. Sumitani, A. Endo, and T. Higashiguchi, *Appl. Phys. Lett.* **91**, 231501 (2007).
- ⁶S. Yuspeh, Y. Tao, R. A. Burdt, M. S. Tillack, Y. Ueno, and F. Najmabadi, *Appl. Phys. Lett.* **98**, 201501 (2011).
- ⁷R. Rakowski, J. Mikołajczyk, A. Bartnik, H. Fiedorowicz, F. de Gaufridy de Dortan, R. Jarocki, J. Kostecki, M. Szczurek, and P. Wachulak, *Appl. Phys. B* **102**, 559–567 (2011).
- ⁸A. Sasaki, A. Sunahara, H. Furukawa, K. Nishihara, S. Fujioka, T. Nishikawa, F. Koike, H. Ohashi, and H. Tanuma, *J. Appl. Phys.* **107**, 113303 (2010).
- ⁹S. Fujioka, H. Nishimura, K. Nishihara, A. Sasaki, A. Sunahara, T. Okuno, N. Ueda, T. Ando, Y. Tao, Y. Shimada, K. Hashimoto, M. Yamaura, K. Shigemori, M. Nakai, K. Nagai, T. Norimatsu, T. Nishikawa, N. Miyanaga, Y. Izawa, and K. Mima, *Phys. Rev. Lett.* **95**, 235004 (2005).
- ¹⁰I. C. E. Turcu and J. B. Dance, *X-Rays from Laser Plasmas: Generation and Applications* (Wiley, West Sussex, England, 1999).
- ¹¹A. Z. Giovannini and R. S. Abhari, *J. Appl. Phys.* **114**, 033303 (2013).
- ¹²R. W. Coons, S. S. Harilal, D. Campos, and A. Hassanein, *J. Appl. Phys.* **108**, 063306 (2010).
- ¹³T. Wu, X. Wang, H. Lu, and P. Lu, *J. Phys. D: Appl. Phys.* **45**, 475203 (2012).
- ¹⁴S. S. Harilal, B. O'Shay, Y. Tao, and M. S. Tillack, *Appl. Phys. B* **86**, 547 (2007).
- ¹⁵J. P. Allain, M. Neito, M. R. Hendricks, P. Plotkin, S. S. Harilal, and A. Hassanein, *Rev. Sci. Instrum.* **78**, 113105 (2007).
- ¹⁶Y. Ueno, G. Soumagne, A. Sumitani, A. Endo, T. Higashiguchi, and N. Yugami, *Appl. Phys. Lett.* **92**, 211503 (2008).
- ¹⁷S. Bollanti, F. Bonfigli, E. Burattini, P. Di Lazzaro, F. Flora, A. Grilli, T. Letardi, N. Lisi, A. Marinai, L. Mezi, D. Murra, and C. Zheng, *Appl. Phys. B* **76**, 277 (2003).
- ¹⁸Y. Tao, M. S. Tillack, S. S. Harilal, K. L. Sequoia, and F. Najmabadi, *J. Appl. Phys.* **101**, 023305 (2007).
- ¹⁹S. S. Harilal, B. O'Shay, M. S. Tillack, and Y. Tao, *J. Phys. D* **39**, 484 (2006).
- ²⁰T. Okuno, S. Fujioka, H. Nishimura, Y. Tao, K. Nagai, Q. Gu, N. Ueda, T. Ando, K. Nishihara, T. Norimatsu, N. Miyanaga, Y. Izawa, K. Mima, A. Sunahara, H. Furukawa, and A. Sasaki, *Appl. Phys. Lett.* **88**, 161501 (2006).
- ²¹H. Komori, Y. Imai, G. Soumagne, T. Abe, T. Suganuma, and A. Endo, "Magnetic field ion mitigation for EUV light sources," *Proc. SPIE* **5751**, 859 (2005).
- ²²A. Endo, H. Hoshino, T. Ariga, T. Miura, Y. Ueno, M. Nakano, H. Komori, G. Soumagne, H. Mizoguchi, A. Sumitani, and K. Toyoda, "Development Status of HVM Laser Produced Plasma EUV Light Source," in Proceedings of the International Sematech EUVL Symposium, Barcelona, 2006.
- ²³S. S. Harilal, B. O'Shay, and M. S. Tillack, *J. Appl. Phys.* **98**, 036102 (2005).

- ²⁴S. S. Harilal, M. S. Tillack, B. O'Shay, C. V. Bindhu, and F. Najmabadi, *Phys. Rev. E* **69**, 026413 (2004).
- ²⁵A. Neogi and R. K. Thareja, *J. Appl. Phys.* **85**, 1131 (1999).
- ²⁶A. N. Mostovych, B. H. Ripin, and J. A. Stamper, *Phys. Rev. Lett.* **62**, 2837 (1989).
- ²⁷C. Plechaty, R. Presura, and A. A. Esaulov, *Phys. Rev. Lett.* **111**, 185002 (2013).
- ²⁸M. S. Rafique, M. Khaleeq-Ur-Rahman, I. Riaz, R. Jalil, and N. Farid, *Laser Part. Beams* **26**, 217–224 (2008).
- ²⁹G. Dimonte and L. G. Wiley, *Phys. Rev. Lett.* **67**, 1755 (1991).
- ³⁰K. Nishihara, A. Sunahara, A. Sasaki, M. Nunami, H. Tanuma, S. Fujioka, Y. Shimada, K. Fujima, H. Furukawa, T. Kato, F. Koike, R. More, M. Murakami, T. Nishikawa, V. Zhakhovskii, K. Gamata, A. Takata, H. Ueda, H. Nishimura, Y. Izawa, N. Miyanaga, and K. Mima, *Phys. Plasmas* **15**, 056708 (2008).
- ³¹T. Suganuma, Y. Ueno, H. Komori, A. Endo, and A. Sumitani, *J. Plasma Fusion Res. Ser.* **8**, 492 (2009), available at http://www.jspf.or.jp/JPFPS/index_vol8-3.html.
- ³²O. Morris, P. Hayden, F. O'Reilly, N. Murphy, P. Dunne, and V. Bakshi, *Appl. Phys. Lett.* **91**, 081506 (2007).
- ³³A. Roy, S. S. Harilal, M. P. Polek, S. M. Hassan, A. Endo, and A. Hassanein, *Phys. Plasmas* **21**, 033109 (2014).
- ³⁴T. Ando, S. Fujioka, H. Nishimura, N. Ueda, Y. Yasuda, K. Nagai, T. Norimatsu, M. Murakami, K. Nishihara, N. Miyanaga, Y. Izawa, and K. Mima, *Appl. Phys. Lett.* **89**, 151501 (2006).
- ³⁵R. Janmohamed, G. Redman, and Y. Y. Tsui, *IEEE Trans. Plasma Sci.* **34**, 455 (2006).
- ³⁶M. Murakami and M. M. Basko, *Phys. Plasmas* **13**, 012105 (2006).
- ³⁷A. Endo, H. Hoshino, T. Suganuma, M. Moriya, T. Ariga, Y. Ueno, M. Nakano, T. Asayama, T. Abe, H. Komori, G. Soumagne, H. Mizoguchi, A. Sumitani, and K. Toyoda, *Proc. SPIE* **6517**, 65170O (2007).
- ³⁸D. B. Geohegan, in *Pulsed Laser Deposition of Thin Films*, edited by D. B. Chrisey and G. K. Hubler (John Wiley & Sons, New York, 1994), p. 115.
- ³⁹P. Mora, *Phys. Rev. Lett.* **90**, 185002 (2003).
- ⁴⁰J. E. Borovsky, *Phys. Fluids* **30**, 2518 (1987).
- ⁴¹C. K. Birdsall and A. Bruce Langdon, *Plasma Physics via Computer Simulation* (McGraw-Hill, 1985).
- ⁴²S. S. Harilal, B. O'shay, and M. S. Tillack, *J. Appl. Phys.* **98**, 013306 (2005).
- ⁴³T. Wu, X. Wang, S. Wang, J. Tang, P. Lu, and H. Lu, *J. Appl. Phys.* **111**, 063304 (2012).
- ⁴⁴See <http://www.cst.com/> for CST Computer Simulation Technology AG.
- ⁴⁵A. Bret and M. E. Dieckmann, *Phys. Plasmas* **17**, 032109 (2010).